Computers and Geotechnics 190 (2026) 107673

Contents lists available at ScienceDirect

Computers and Geotechnics

journal homepage: www.elsevier.com/locate/compgeo

Research paper

A novel constitutive model for double-twisted hexagonal meshes within the Macroelement framework

Marco Previtali [a,c,*], Matteo Oryem Ciantia [a,b], Giovanni Battista Crosta [b]

[a] School of Science and Engineering, University of Dundee, Small's Lane, Dundee, DD1 4HR, United Kingdom
[b] Department of Earth and Environmental Sciences, University of Milano-Bicocca, Piazza della Scienza, 4, Milan, 20126, Italy
[c] Multi-physics and Multi-scale Modelling Lab, Westlake University, No. 600 Dunyu Road, Hangzhou 310030, Zhejiang Province, China

ARTICLE INFO

Dataset link: https://github.com/marcoprevitali/macroelement-doubletwist-PFC7, https://zenodo.org/records/17299219

Keywords:
Flexible barrier
Multi-scale model
Macroelement
Double-twisted mesh

ABSTRACT

This paper presents a novel model for simulating double-twisted hexagonal wire meshes, commonly used in both active and passive rockfall barriers. The mechanical behaviour of the wires is first investigated through laboratory tests, which are then used to calibrate and validate a high accuracy continuum representation of the wire interweave. This model enables the analysis of the response of the wire mesh to loading conditions that can be difficult to obtain experimentally. The resulting data is used to develop a define the equations of a Macroelement model, which efficiently translates the insight from the wire to the barrier scale, improving the overall accuracy without compromising computational efficiency. Natural variability in the barrier response is introduced through a parameter correlation approach. Finally, the model is evaluated against standard literature approaches through simple boundary value problems.

1. Introduction

Wire meshes are a common mitigation measure for rockfall due to their low cost and ease of installation (Volkwein et al., 2011). While international guidelines (EOTA, 2013) prescribe standardised testing conditions across manufacturers, they do not provide information on the barrier response to edge cases, such as non-spherical rock blocks or impacts near the fence posts. Due to the significant cost of field tests, numerical models are employed to investigate the barrier interaction with complex natural hazards (Li and Zhao, 2018; Albaba, 2015). While some authors are now explicitly modelling the geometry of steel meshes (Escallón et al., 2015; Li et al., 2020; Xu et al., 2018; Albudairi et al., 2016), a multi-scale approach is generally preferred for large panels of small sieve sized meshes due to its computational efficiency: the mesh is represented as an assembly of spring-like elements that replicate the desired wire-scale behaviour (Effeindzourou et al., 2017; Li and Zhao, 2018; Pol et al., 2021). This approach has been implemented in both Continuum (Finite Element Method, FEM) and Discrete (Discrete Element Method, DEM) frameworks, using beam and truss elements (Mentani et al., 2016); and remote bonds between particles (Previtali et al., 2020b; Bertrand et al., 2008), see Fig. 1b. Membrane formulations, used for active barriers, can also be considered part of the multi-scale approach (Lambert and Bourrier, 2024; Boschi et al., 2023).

Double-twisted hexagonal meshes are particularly suited for this multi-scale approach as explicitly representing the wire geometry is computationally demanding due to the small sieve size and the significant resolution required to capture the twisting behaviour (Previtali, 2023). While these meshes are now typically used in combination with other mesh models (e.g. steel rings and strand ropes), they remain one of the most widespread designs, employed in both active (Pol and Gabrieli, 2021) and passive structures (Marigo et al., 2021; Previtali et al., 2021c). The design consists of two wires intertwined for one and half turns each, forming a repeating hexagonal pattern (Fig. 1a). This configuration strengthens the mesh, minimises the risk of unravelling in the event of wire failure and reduces the stress localisation at the wire–wire interface (Escallón et al., 2015; Bertrand et al., 2008). In the numerical representation, separate responses are assigned to single-wires (SW) and double-twists (DT), typically by means of piecewise linear force–displacement curves. The mechanical behaviour of SW is derived from experimental tests, while for DT, it is obtained using a simplified analytical framework (Bertrand et al., 2008) or again measured experimentally (Thoeni et al., 2013). However, as this approach only defines the axial tensile response, shear and bending behaviour are left to the arbitrary choice of the modeller. Some authors prescribe negligible bending and compressive stiffness (Thoeni et al., 2013; Pol and Gabrieli, 2021), while others assume that the wire behave as an

* Corresponding author at: School of Science and Engineering, University of Dundee, Small's Lane, Dundee, DD1 4HR, United Kingdom.
E-mail address: m.z.previtali@dundee.ac.uk (M. Previtali).

https://doi.org/10.1016/j.compgeo.2025.107673
Received 14 April 2025; Received in revised form 23 August 2025; Accepted 25 September 2025
Available online 11 October 2025

Euler beam (Li and Zhao, 2018; Albaba et al., 2017). Both approaches have their limitations: neglecting shear stiffness produces minimal resistance until all wires are loaded, producing a smooth deformation field. While this configuration is able to capture standard field tests, as current guidelines prescribe idealised centred impacts (EOTA, 2013); it prevents localised loading and failure mechanisms, critical for simulating the so-called bullet effect, a phenomenon that occurs when small, high-velocity blocks pierce the barrier at kinetic energy levels below the design threshold (Mentani et al., 2016; Spadari et al., 2012). On the other hand, simply using an Euler-beam approach to compute the shear behaviour overestimates the overall mesh stiffness, as plastic work can only occur under tensile deformations. In this context, plasticity can be modelled by extrapolating the uniaxial elasto-plastic response (from the SW curve) and integrating it across the wire cross-section using a fibre discretisation approach (Mijalković et al., 2008), capturing distributed yielding and hardening effects under combined loading (Previtali, 2023). However, this approach requires a-priori knowledge of the strain distribution across the wire, which is difficult to obtain for the double-twisted interweave, and it is inefficient to solve at runtime.

Given these limitations, this paper aims to provide a novel constitutive model for double-twisted hexagonal meshes under generalised loading conditions. The idea is to use an accurate but computationally expensive Finite Element Model (FEM) to characterise the response of the intertwined wire pieces subject to various loading conditions, and then to approximate this behaviour using a more efficient formulation, the macroelement. Finally, the macroelement description of the wire-scale behaviour is implemented as a contact law in a discrete element method (DEM) code, to obtain an accurate mesh response without explicitly simulating the geometric interaction of each piece of wire.

2. Model development

The development procedure is constituted by three phases: (i) calibration of the high-accuracy model against wire-scale laboratory tests, (ii) the use of this high accuracy model to explore the wire response to various loading conditions and (iii) use of the combined experimental and high-accuracy FEM results to define the equations that approximate the observed model response.

2.1. Laboratory testing

The development and calibration of the high-accuracy FEM model is based on the mechanical response of the steel wires to tensile, compressive and three point bending tests, by means of an Instron 4204 tester. The DT mesh is constituted by zinc-polymer coated steel wires, used in passive protection structures. Fig. 1 provides the reference geometry: L_{sw} is 6 cm, L_{dt} is 3.5 cm and wire diameter is 3 mm. The angle between the DT and SW orientations ranges from ≈ 30 to ≈ 45 degrees. Single-wire portions are separated from the mesh by cutting ≈ 5 mm away from the start of the DT interweave. Laboratory tests are also carried out on PVC-sheathed mild steel wires used in rock gabions, showing a similar response; data available in Previtali (2023).

Three types of tests are carried out: (i) tensile, (ii) compressive and (iii) three-point bending. Tensile tests represent the bulk of the laboratory data and are carried out to characterise the material behaviour (for single-wires) and the intertwinement-scale response (for double-twists). Compressive tests are used to exclude non-symmetric tensile-compressive stiffness (for single-wires) and to measure the failure/buckling load (for double-twists). Finally, three-point bending testing is only carried out on double-twists and it is used to provide verification data for the numerical model.

2.1.1. Tensile testing

All tests are carried out under displacement-controlled loading at a rate of 2 mm/min, following a preliminary study that exhibited no rate effects (Previtali, 2023). Single-wire pieces are fixed using wedge-action tensile grips, with an initial wire-grip overlap length of ≈ 15 mm. Due to the size limitations of these tensile grips, an additional mechanical support, constituted by two steel plates with 1.5 mm deep rounded grooves oriented at a 45 degrees angle (Fig. 2a) is used to test the Double-twist interweaves. In both cases, the confining pieces are gently tightened with bolts, to avoid damaging the wires at the interface with the confining object. This weak coupling results in significant wire slippage (≈ 50% of total displacement), corrected through a combination of a local extensometer and image analysis (Previtali et al., 2021a; Previtali, 2023).

Wire failure occurs due to well-distinct mechanisms of necking in the SW and shearing at the DT extremities (Figs. 2b,c). Fig. 3 shows the resulting force–displacement curves. Overall, the SWs exhibit significant variability in peak force and deformation at failure. This is attributed to spurious plastic strains developed during manufacturing and storage: as the test does not induce wire failure at specific locations, pre-existing defects govern the onset of necking.

The DT test exhibits a different response: first, the experimental setup induces wire failure at a specific location, i.e. the connection between DT and SWs. Once a wire fails, the DT interweave is pulled by the other three wires and the test ends, so that the measured force corresponds to the failure threshold of the weakest of the four wires, reducing the overall variability in the system response. Assuming that the experimental DT setup splits the total force into equal parts, the wires fail in shear at ≈ 60%–70% of the load required for necking. Another peculiarity is given by the initial portion of the DT force–displacement curve, governed by the frictional sliding of the wires. While initially loose in the experimental configuration, they tighten as the DT gets pulled, until friction inhibits movement, sliding stops and elasto-plastic behaviour takes over. Since the zinc-polymer coated wires used here are characterised by low static friction (Mitterer et al., 1997), the transition from sliding to elastic regime is smooth, and the overall shape of the curve is governed by the initial wire configuration. This is corroborated by the tests carried out on PVC-sheathed wires, characterised by significant static friction: the force–displacement curve exhibits a stick–slip response and the initial wire configuration (and its variability) has a lesser effect on the overall curve (Previtali, 2023).

2.1.2. Other tests

Compressive tests are carried out to exclude unexpected material behaviour, such as a different yield strength of the material in tension and compression. As seen in Fig. 3c, this results in a buckling failure at ≈ 1.3–1.6 kN for the single-wire and wire unravelling at 300–350 N for the double-twist.

A three-point-bending test was carried out on the double-twist to provide validation data for the high-accuracy model: two steel cylinders, with a diameter of 4 cm, are used as support pins, positioned at a distance of ≈ 5 cm apart from each other. This produces four separate contact points between the pins and the wire extremities, preventing the DT from rotating around its axis. The centre of the DT was loaded with a semi-circular surface (3.5 cm diameter). Since this test is not used to provide information on the mechanical behaviour of the material and it is only used to validate the numerical model, the data is plotted together with the numerical curve in the next section.

2.2. High-accuracy model (FEM)

A Finite Element model of the double-twist interweave is developed to simulate the wire's behaviour under combined bending and tensile conditions, difficult to replicate experimentally, to provide a calibration dataset for the macroelement. The mechanical properties of the material are derived from the experimental SW tests (Fig. 3a), while the results of tensile DT tests (Fig. 3b) are used to verify the intertwinement-scale response of the model. The results of compressive tests are not used to calibrate or validate the FEM model. The code

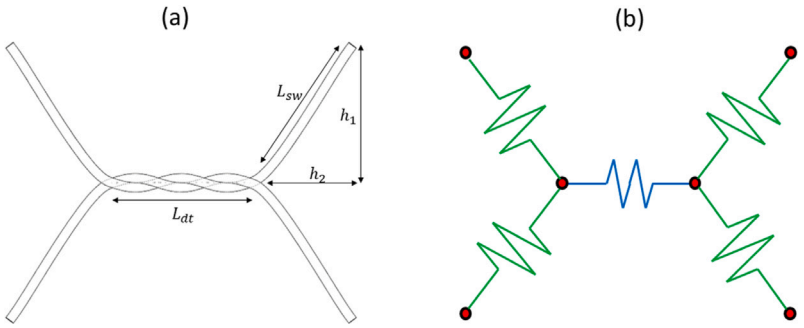

Fig. 1. (a) Hexagonal mesh wire geometry. The double-twist (DT) in the centre is connected to four single-wires (SW); (b) discretisation adopted for the numerical model. The red dots represent the DEM particles, connected by springs of different stiffness.

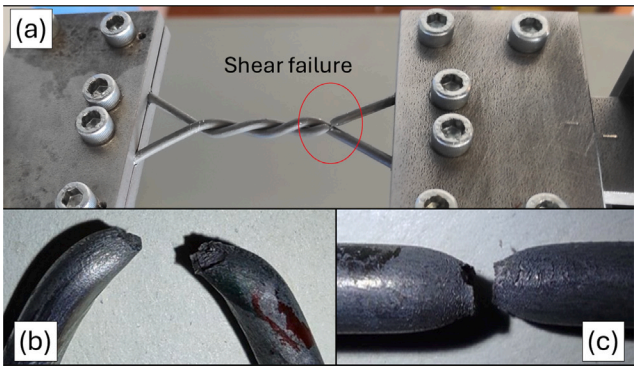

Fig. 2. Tensile testing of double-twists. (a) Shear failure develops at the edges of the DT. Zoom on the failed wire pieces in (b) shear and (c) necking.

ABAQUS CAE is employed to its scripting interface and capability to handle large-deformations and contact interactions. Once the model is validated, 10 load paths are used to characterise the tensile behaviour of the wire, by interpolating between pure tensile and pure bending conditions. The same is done for compressive behaviour, interpolating between pure bending and pure compression. This is done for both single-wires and double-twists, resulting in a total of 40 simulations. The raw results data is shown in Previtali (2023).

2.2.1. Material model

The constitutive model is isotropic linear elastic, with a Von Mises yield surface, associated flow-rule and ductile and shear damage functions, entirely calibrated on the experimental single-wire tensile tests (Fig. 3a). After calibration, the constitutive model is used to simulate both single-wires and double-twist geometries. The rate-independent plastic hardening model is defined through piecewise linear interpolation (Abaqus, 2011). The experimental tensile SW curves are first converted to true stress–plastic strain data ($\sigma - \varepsilon^{pl}$), averaged and then resampled with 20 points (Previtali, 2023).

Ductile softening and failure are reproduced with a damage-based approach, linearly scaling stress as function of damage. This is expressed using an energy-based formulation, where G_f is the area subtended by the experimental $\sigma - \varepsilon^{pl}$ curve between the plastic strains associated with damage onset ($\bar{\varepsilon}_0^{pl}$) and wire failure ($\bar{\varepsilon}_f^{pl}$). A characteristic length parameter L_c is used to link the energy formulation to the measured wire displacement (Eq. (1)), mitigating mesh dependency. This value is set equal to the necking zone width measured during the SW tensile test (5 mm). It is important to note that the damage model is set as a homogeneous material behaviour, and it is not applied to random elements within the finite element model as it would be for a random field approach. The assumption is that failure always occurs at the interface between single-wire and double-twist, and therefore setting a random field variable in different regions of the geometry would have limited influence.

$$G_f = L_c \int_{\bar{\varepsilon}_0^{pl}}^{\bar{\varepsilon}_f^{pl}} \sigma d\bar{\varepsilon}^{pl} \tag{1}$$

The reference stress ratio $q/p = (\sigma_1 - \sigma_3)/(\sigma_1 + 2\sigma_3)/3$ is set to 3 as the wires were tested under unconfined conditions ($\sigma_{2,3} = 0$). The shear damage model is not calibrated on experimental shear data, since no such tests were carried out. Instead, the model parameters are derived from the ductile damage model by applying a conversion factor of 0.6, which matches both literature data (Shigley et al., 1972) and the experimental observation of failure occurring at ≈ 60% of the value observed in SW tests. Additional details are available in Previtali (2023).

2.2.2. Double-twist model

The double-twist geometry (Fig. 1a) is reproduced using a parametric design approach, previously tested in Previtali (2023) on experimental data from Thoeni et al. (2013): a circular section of diameter $D = 3$ mm is swept along the rail curve, i.e. an helix of the same radius and with a curvature of $3\pi/L_{dt}$ (Fig. 4b). The pitch angle of the interweave is defined as the angle between the wire cross-section and the double-twist orientation (Fig. 4a). This value is here set to 19 degrees after previous back-calibration studies (Previtali, 2023). The second wire is generate through point-symmetry at its centre. The SW pieces at the extremities of the double-twist are blended with a bulge factor of 0.1 and continuity of the curvature (Fig. 4c), where the bulge factor is defined as the tangent of 1/4th of the included angle of a curved segment (Gossling, 1981). These two geometric factors were identified through an iterative procedure, by simulating the experimentals DT test and minimising the difference in axial stiffness and failure stress (Previtali, 2023). Wire–wire contacts are addressed using symmetric master–slave surfaces interactions and finite sliding (Steinbrecher et al., 2017). By definition, the master surface is rigid and overlaps with the deformable slave surface, which adjusts to accommodate the imposed displacement. Since neither wire is inherently stiffer than the other, symmetric contact conditions are applied to ensure that both wires deform minimising internal work. The penalty method is used to enforce contact constraints, with a friction coefficient of 0.3 [−] applied in the tangential direction.

2.2.3. Geometry discretisation and boundary conditions

The wire geometry is discretised using a hexahedra-dominated mesh with second-order elements (C3D15 and C3D20) of length $L = 0.5$ mm. As these element types do not possess rotational degrees of freedom, wire bending is prescribed as nodal displacement through an user-defined Fortran subroutine (DISP.f). Axial displacement is imposed up to 50% of the initial wire length and bending up to a rotation of 45 degrees. For the axial pull, fixity conditions are applied at the extremities of the SWs. In the three-point-bending test, three contacting bodies with the same curvature of the experimental objects are

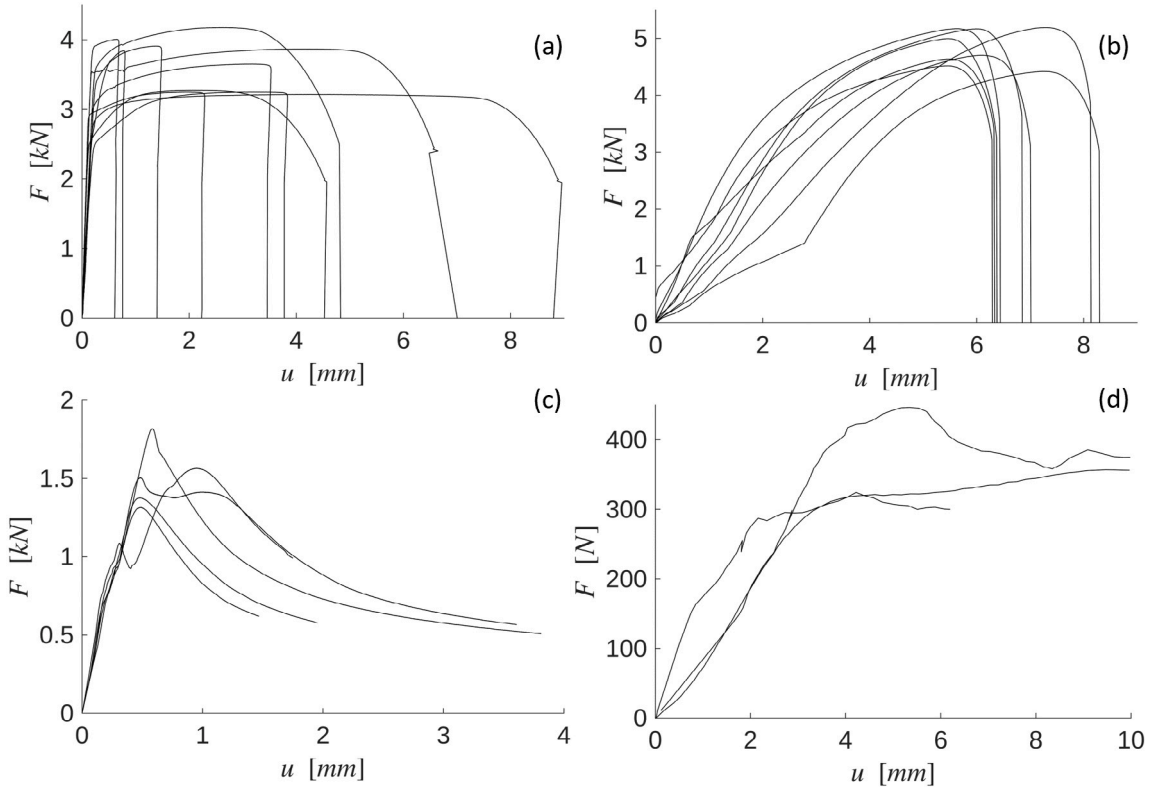

Fig. 3. Uniaxial testing of the mesh. Tension (a) SW, (b) DT; Compression (c) SW, (d) DT.

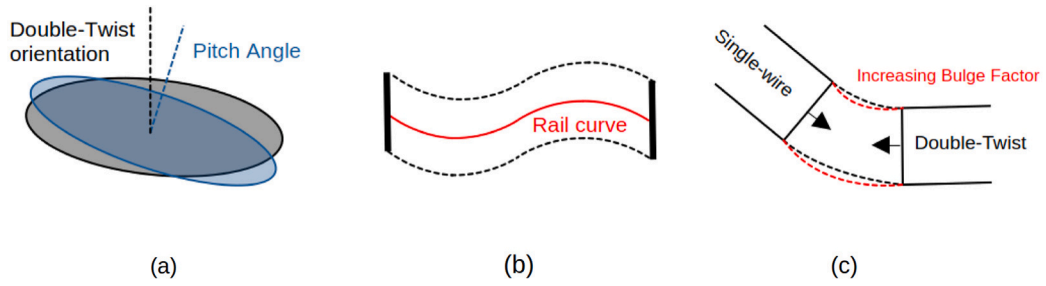

Fig. 4. Definition of the double-twist geometry: (a) pitch angle of the wire cross-section with respect to the double-twist orientation, (b) extrusion of the cross-section along the rail curve, (c) interpolation between single-wire and double-twist orientation through bulging.

employed. A single node in the centre of the double-twist is fixed in the out-of-plane direction to avoid zero-energy mode translation due to under-constraining. The comparison between experimental and numerical data for the axial tension and bending tests is shown in Fig. 5. After the model is calibrated and validated, the effective force–displacement curves used for the macroelement are obtained by applying a larger displacement at the SWs extremities and extracting the stresses and displacements at their contact with the DT.

2.3. Macroelement model

The macroelement is a numerical approach used to reduce computational burden by approximating the mechanical behaviour of a system, typically soil–structure interactions (Nova and Di Prisco, 2003), into a single numerical object. In practice, it is a standard constitutive model applied to a pre-defined geometry and therefore expressed directly in terms of generalised forces (F, M) and displacements (u, ω). The formulation adopted here involves all the typical ingredients of classic elasto-plastic models: (i) a constitutive equation, linking forces and displacements, (ii) a yield surface f in the generalised forces space defining the transition to elasto-plastic behaviour. The yield surface expands through (iii) isotropic hardening laws as a function of non-reversible plastic deformations (u_{pl}, ω_{pl}). During plastic integration, the non-reversible deformation increment (plastic multiplier $\dot{\lambda}$), is split between axial and rotational portions according to (iv) the plastic potential function g. Necking and shear failure are lumped into a simplified (v) damage model. Finally, the initial low-stiffness response of the double-twist is simulated using an (vi) in-series non-linear spring model.

2.3.1. Elastic model

Standard beam behaviour, used to represent the wires (Previtali et al., 2020a), is expressed in incremental form as:

$$\delta F = \delta u \cdot EA \tag{2}$$

$$\delta M = \delta \omega \cdot EI \tag{3}$$

where u, ω and EA, EI are respectively the axial/rotational deformations and stiffnesses. The latter are measured from pure tensile and simple bending tests (see Tables 1,2). These values are here used directly, i.e. without separating material and geometric components,

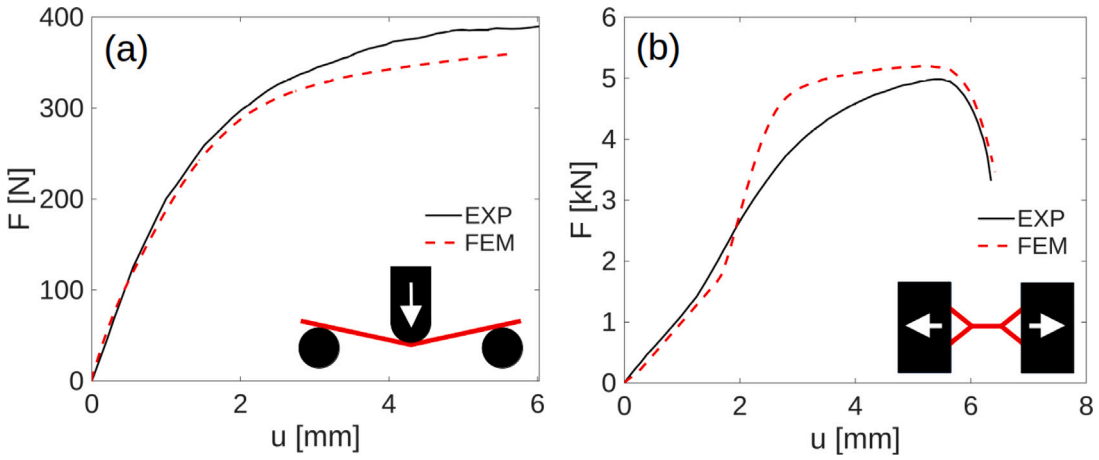

Fig. 5. Comparison of data from an individual test experimental and FEM data: (a) Force–displacement curve for the upper loading roller in the three-point DT bending test. The experimental curve shown is the dataset with the median value of force at 6 mm displacement, although the tests exhibited minimal variability (< 4% across 5 tests). (b) Force–displacement curve for the axial DT pulling test. The full range of experimental curves is shown in Fig. 3b.

as the second moment of the cross-section area (I) of the double-twist, calculated under the assumption of small deformations, does not match the one measured experimentally (Previtali, 2023).

2.3.2. Simplified wire-sliding model

The non-linear low stiffness observed in the first portion of the DT force–displacement curve (Thoeni et al., 2013), is modelled in uniaxial tension as a reversible non-linear relationship. This function therefore needs an exponential growth to match the experimental data, and to reach asymptotically the elastic model stiffness EA. This can be achieved by modelling sliding as in-series springs ($K_{sliding}$): given Eq. (4), the resulting spring K_{eq} becomes equivalent to the elastic model EA at $K_{sliding} \gg EA$. While any exponential curve can be used for this, its fitting would depend on both the target elastic stiffness EA and the displacement at which the transition occurs, coupling the two effects and making it difficult to define a clear physical meaning to its parameter. On the other hand, the rational function adopted here (Eq. (5)) has the added advantage of explicitly prescribing the interlocking displacement u_d and decoupling it from the hardening parameter a_s, which governs the transition sharpness from sliding to locking. Additionally, a_s can be calculated using Hertzian contact theory as described in the appendix (Johnson, 1987).

$$\frac{1}{K_{eq}} = \frac{1}{K_{sliding}} + \frac{1}{EA} \tag{4}$$

$$K_{sliding} = a_s/(u_d - u) \tag{5}$$

2.3.3. Yield surface

The yield surface, its parameters and hardening function are obtained by fitting the radial load path inflection points in $F - \tilde{M}$ space, with $\tilde{M} = M/D$ and D being the wire diameter. The emerging shape features a peak at zero force ($F = 0$), as combined load induces yielding at lower values than pure tension or bending (Fig. 6). The equation chosen to capture this must be convex and C^2 continuous within the parameter space and possess axes-orthogonal derivatives at their intersection, i.e. $f'(F = 0) \to \infty$ and $f'(M = 0) = 0$, to avoid non-physical behaviour such as uniaxial tension causing wire bending. The formulation adopted here is the sum of an exponential (Eq. (6)) and a quadratic curve (Eq. (7)). The original formulation by Gerolymatou (2017) is defined in the range $[0, N_f]$ on the x-axis, with N_f being the size of the yield surface and M_f, α and β being its shape parameters. The exponential part, Eq. (6), is used to control the skewness (through α) and the curvature (through β) of the resulting surface, while Eq. (7) controls the ratio between axial and bending strength (through M_f). Eq. (6) has a local maximum ($h = 1$) at $F/N_f = \alpha$ and two asymptotic minima ($h \to 0$) at $|F/N_f - \alpha| \gg 0$. Therefore, to obtain a local peak at $F = 0$, axis translation is performed (Eq. (8)). As shown in Fig. 6, the best-fit surfaces in the initial state and at peak expansion exhibit limited variations in shape, and the parameter chosen here (Tables 1, 2) are those associated to the former.

$$h = exp\left[-\frac{1}{\beta}\left(\frac{F^*}{N_f} - \alpha\right)^2\right] \tag{6}$$

$$f = \tilde{M}^2 + M_f h\left(F^* - N_f\right)F^* \tag{7}$$

$$F^* = F + N_f/\alpha \tag{8}$$

Two approaches can be employed to define the modulus of the axis-translation: (i) by setting the compressive limit N_T as a constant (e.g. the buckling limit) and expressing α as a function of the other variables (i.e. Eq. (9)), with the constraint of function peak at $F = 0$ or (ii) by adopting a constant α and substituting the compressive portion with a different function, i.e. a multi-surface formulation (Previtali, 2023).

$$\alpha = \frac{F^*}{N_f} + \sqrt{\beta}\sqrt{\log\frac{\tilde{M}^2}{M_f(N_f - F^*)F^*}} \tag{9}$$

It is important to note that Eq. (9) is highly sensitive to small increments in F^* for certain parameter combinations (particularly near $F^* = 0$ or $F^* = N_f$), and using α as a dependent variable complicates fitting highly skewed data (e.g., $N_f/2 \gg |F_t|$, Fig. 6b). Therefore, the constant α approach (specifically centred at the origin, $\alpha = 0.5$) is adopted here.

The resulting surface is geometrically similar to a superellipse (Lamé curve, Eq. (10)). In fact, β and M_f have respectively the same roles as n and b/a in Eq. (10). However Eq. (7) offers computational advantages for the problem at hand: the single-wire yield surface is characterised by low curvature (Fig. 6a), as established by the analytical solution for circular cross-section beams (Di Laora et al., 2020; Previtali, 2023). Capturing this behaviour with a superellipse requires $n \to 1$, introducing an abrupt derivative changes at $M \to 0$, i.e. the loading scenario most common during rockfall impact. On the other hand, Eq. (7) provides a smoother transition to axis-orthogonal derivatives at $M \to 0$, enabling larger sub-stepping sizes during error-controlled numerical integration (see Appendix). A standard ellipse ($n = 2$) is used for the region of compressive force $F < 0$, as it is an uncommon loading scenario and this simple formulation matches adequately.

$$\left|\frac{F}{a}\right|^n + \left|\frac{M}{b}\right|^n = N_f \tag{10}$$

The yield limit in compression N_T is defined after comparing experimental data, numerical results and the closed-form solution for the

Table 1
Macroelement model, Single-wire parameters.

	Physical meaning	Unit	Mean	CV	Calibration
EA	Axial Stiffness	N/m	1.78E+7	0.38	Tensile test (EXP)
EI	Bending Stiffness	N/m^2	1.22E−1	0.38	Bending test (FEM)
L	Wire Length	m	6.00E−2	0.0	Measured
N_0	Tensile yield strength	N	2.75E+3	0.13	Tensile test (EXP)
N_1	Maximum tensile force	N	3.74E+3	0.09	Tensile test (EXP)
N_T	Compressive yield strength	N	1.65E+3	0.15	Compressive test (EXP)
M_f^f	Shape parameter	–	2.85E−2	0.0	Combined loading (FEM)
α^f	Shape parameter	–	0.5	0.0	Combined loading (FEM)
β^f	Shape parameter	–	1.94E−1	0.0	Combined loading (FEM)
k_F	Inverse of characteristic displacement	m^{-1}	2.39E+3	1.68	Tensile test (EXP)
k_M	Inverse of characteristic rotation	deg^{-1}	1.12E−1	1.68	Bending test (FEM)
M_f^g	Plastic potential shape	–	4.78	0.0	Combined loading (FEM)
α^g	Plastic potential shape	–	2.55	0.0	Combined loading (FEM)
β^g	Plastic potential shape	–	3.58E−2	0.0	Combined loading (FEM)
W_{pl}^1	Damage onset threshold	J	6.37	0.63	Tensile test (EXP)
W_{pl}^2	Mesh failure threshold	J	1.1E+1	0.79	Tensile test (EXP)
α	Damage scaling factor	–	4.97	1.36	Tensile test (EXP)

Table 2
Macroelement model, Double-twist parameters.

	Physical meaning	Unit	Mean	CV	Calibration
EA	Axial Stiffness	N/m	3.99E+6	0.28	Tensile test (EXP)
EI	Bending Stiffness	N/m^2	2.57E−1	0.28	Bending test (FEM)
L	Wire Length	m	3.50E−2	0.0	Measured
N_0	Tensile yield strength	N	2.81E+3	0.1	Tensile test (EXP)
N_1	Maximum tensile force	N	5.01E+3	0.06	Tensile test (FEM)
N_T	Compressive yield strength	N	3.20E+2	0.03	Compressive test (EXP)
M_f^f	Shape parameter	–	3.54E−2	0.0	Combined loading (FEM)
α^f	Shape parameter	–	0.50	0.0	Combined loading (FEM)
β^f	Shape parameter	–	6.42E−2	0.0	Combined loading (FEM)
k_F	Inverse of characteristic displacement	m^{-1}	4.08E+3	0.46	Tensile test (EXP)
k_M	Inverse of characteristic rotation	deg^{-1}	2.64E−1	0.46	Tensile test (EXP)
M_f^g	Plastic potential shape	–	6.32E−4	0.0	Combined loading (FEM)
α^g	Plastic potential shape	–	0.50	0.0	Combined loading (FEM)
β^g	Plastic potential shape	–	3.24	0.0	Combined loading (FEM)
W_{pl}^1	Damage onset threshold	J	1.25E+1	0.29	Tensile test (FEM)
W_{pl}^2	Mesh failure threshold	J	2.21E+1	0.19	Tensile test (FEM)
α	Damage scaling factor	–	4.62E−1	0.16	Tensile test (FEM)
a_s	Wire tightening coefficient	–	2.52E+3	0.56	Tensile test (EXP)
u_d	Mesh distortion	m	1.0E−3	0.71	Tensile test (EXP)

buckling of thin Euler beams with both ends fixed. The analytical buckling limit is 5.75 kN, meaning the wire would undergo material yielding ($F \approx 2.7$ kN) far before buckling, which is also what is observed in the FEM results (Previtali, 2023). The experimental curves exhibit an even lower peak force ($F \approx 1.6$ kN, Fig. 3c), which is assumed to be due to wire defects and experimental limitations (e.g. grip misalignment). As the analytical solution for a beam pivoted at both sides gives a similar value ($F = 1.44$ kN) and so do the hybrid bending/compression FEM tests, this value was chosen to represent the buckling limit in the macroelement model. For the double-twists, the force measured in the experimental test due to unravelling ($\approx$ 340 N) is adopted. Still, this value is of lesser importance in double-twists as the wire-sliding model already captures the unravelling phenomenon, accommodating the compressive displacement.

2.3.4. Hardening function

The yield surface size (Eq. (11)) is obtained by interpolating between the prescribed initial (N_0) and peak (N_1) surfaces through the hardening variable η.

$$N_f = N_0 + \eta(N_1 - N_0) \tag{11}$$

From Eq. (7), N_0 and N_1 are the yield and peak forces measured in the uniaxial tensile test. The non-linear portions of the experimental curves (Figs. 3a,b) are thereby normalised and fitted considering η as dependent variable and the non-reversible plastic deformations as independent. As discussed in Previtali (2023), a variety of equations can be used in this step, as shown in the appendix. A negative exponential function, Eq. (12), characterised by a single fitting parameter per hardening variable (k_F) provides a decently accurate approximation ($R^2 \simeq 0.95$). Better results ($R^2 > 0.99$) can be obtained using rational functions (Previtali, 2023). Alternatively, substituting individual plastic variables for dissipated energy (W_{pl}) provides a more robust model for combined loading, at the expense of accuracy ($R^2 \simeq 0.9$), as the function has to fit a higher-dimension problem. Eq. (12) is adopted here for simplicity as the resulting error is lower than the natural variability observed in the experimental data and it was historically used to model the plastic hardening behaviour of metals (Thomson, 1865). The same procedure was carried out for k_M using the FEM data from Previtali (2023). The two fitting parameters (k_F and k_M) represent the normalised initial stiffness coefficients of the non-linear hardening curve, also known as the inverse of the characteristic displacement ($1/k$ is the generalised displacement that corresponds to $\eta = 0.63$).

$$\eta = 1 - exp\left(-k_F|u_{pl}| - k_M\omega_{pl}\right) \tag{12}$$

The non-reversible plastic displacement u_{pl} and rotation ω_{pl} are obtained from the FEM results through strain decomposition.

$$u_{pl} = u - u_{el} = u - F/EA \tag{13}$$

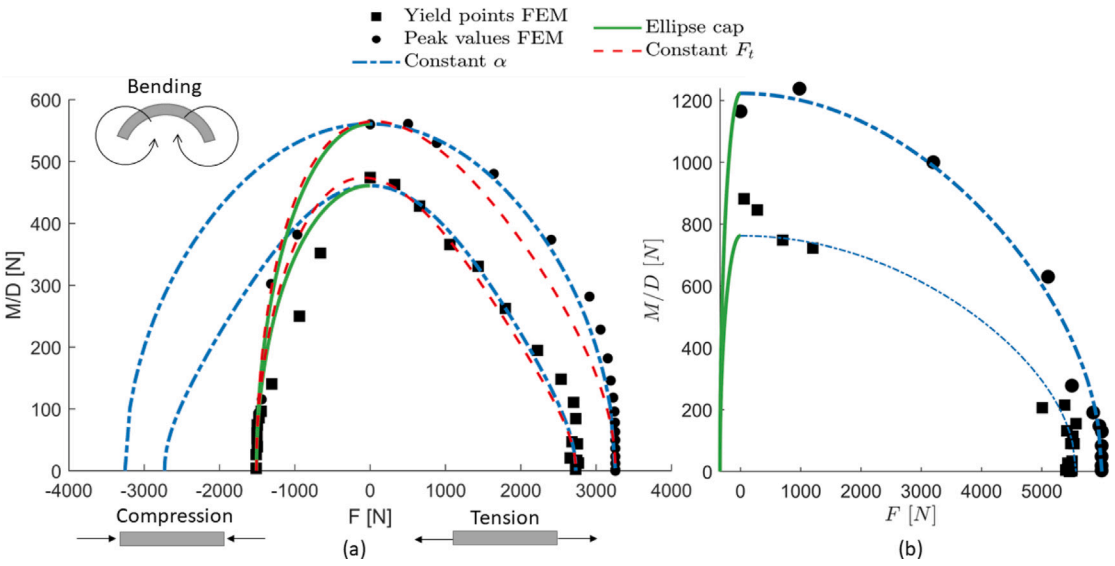

Fig. 6. Yield surfaces (at the initial state and peak expansion) fitted on FEM data. (a) single-wire, (b) double-twist. Fewer points are available for the latter due to spurious unravelling behaviour during hybrid bending–pulling conditions, making it difficult to identify material yielding. Eq. (23) (constant N_T) is not shown for the double-twist due the significant skewness of the data, i.e. $\alpha \to 0$.

$$\omega_{pl} = \omega - \omega_{el} = \omega - M/EI \tag{14}$$

2.3.5. Plastic potential

Given generalised forces $\boldsymbol{F} = [F, M]$ and displacements $\boldsymbol{u} = [u, \omega]$, the plastic potential function g is defined so that:

$$\dot{\boldsymbol{u}}_{pl} = \dot{\lambda} \cdot \partial g / \partial \boldsymbol{F} \tag{15}$$

Eq. (7) is again used to fit the FEM results due to its C^2 continuity and versatility. First, $\dot{\boldsymbol{u}}_{pl}$ is obtained at each data point of the FEM dataset according to Eqs. (13) and (14). Since these plastic increments have different dimensions (i.e. distance and rotation), they are normalised by the total increment at the given FEM step (e.g. $\bar{u}_{pl} = \dot{u}_{pl}/\dot{u}$), so that their sum equals one. This normalisation has the added advantage of removing the plastic multiplier $\dot{\lambda}$ from Eq. (15). To further simplify the calibration, plastic flow is expressed as their ratio, i.e. $\bar{\omega}_{pl}/\bar{u}_{pl}$. The best fitting parameters (α^g, β^g, M_f^g, Eqs. (6) and (7)) for the chosen plastic potential function are the obtained by minimising the difference between the normalised plastic increment ratio at a given $\boldsymbol{F}$ (obtained from FEM) and the ratio of the function derivatives, i.e. Eq. (16). Here, only the plastic increments between $0 < W_{pl} < W_{pl}^1$ are employed. For the double-twist, due to the additional noise due to wire sliding, $\tilde{M}/F < 0.4$ and > 2 are discarded, under the assumption that the function derivatives are assumed to be orthogonal to the axis.

$$\min_{\alpha^g, \beta^g, M_f^g} \left| \frac{\partial g}{\partial \boldsymbol{F}} - \frac{\bar{\omega}_{pl}}{\bar{u}_{pl}}(\boldsymbol{F}) \right| \tag{16}$$

The simplex algorithm (Lagarias et al., 1998) is here used instead of standard least-square minimisation as imaginary values can emerge during unconstrained optimisation of Eqs. (6) and (7). The resulting trends are linear (Fig. 7a) and exponential (Fig. 7b). Associated plastic flow is used for wire compression.

2.3.6. Damage model

The tangential stiffness modulus of the wires goes to zero as $\eta \to 1$ (Eq. (12)), making convergence difficult. In the literature, this is prevented by deleting the affected wire at a specific threshold of total (Thoeni et al., 2013) and plastic strain Mentani et al. (2016) or force (Effeindzourou et al., 2017). Here, a standard power-law damage evolution model (Simo and Ju, 1987) is used to capture ductile failure without having to rely on yield surface shrinkage, which can cause overshooting issues (Huang and Griffiths, 2009).

$$\dot{W}_{pl} = \dot{u}_{pl} F + \dot{\omega}_{pl} M \tag{17}$$

$$\delta = \left(\frac{W_{pl} - W_{pl}^1}{W_{pl}^2 - W_{pl}^1} \right)^{\alpha} \tag{18}$$

$$\bar{\mathbf{F}} := \bar{\mathbf{F}} \cdot (1 - \delta) \tag{19}$$

Where δ is the normalised damage parameter and α is the damage exponent. The two thresholds define the start of necking and shearing (W_{pl}^1) and the actual wire failure (W_{pl}^2). If $\alpha \ll 1$, the resulting force has a sudden drop, typical of brittle materials. At $\alpha = 1$, there is a linear degradation, while for $\alpha \gg 1$, the resulting force initially decreases gradually and then exhibits a rapid loss, as it is observed in the shearing and necking failure of wires (see Fig. 3). The thresholds, typically defined using plastic strain in continuum mechanics, are here expressed as dissipative plastic work (W_{pl}, Eq. (17)) to obtain a consistent response under combined loading and generalised forces–displacements.

2.4. Parameters summary and variability

The variability of the mechanical response is implemented by assigning random values to each parameter within a prescribed distribution (Fig. 8) (Thoeni et al., 2013). To ensure that the parameters assigned to an individual wire are physically meaningful, one parameter is chosen as the independent variable j. The remaining parameters are then derived as a weighted combination of random sampling and their linear correlation with the independent variable, i.e. the Pearson coefficient ρ:

$$p_i = \frac{\sigma_i}{\sigma_j} \rho_{ij} (x_j - \tilde{x_j}) + \left(1 - \rho_{ij}\right) x_i \tag{20}$$

where p is the assigned value for the ith parameter, x is a randomly sampled value within its distribution of standard deviation σ_i and $\tilde{x}_j$ is the median value of the reference parameter.

The correlation between each parameter is explored in Fig. 9: for the single-wires (upper triangular matrix portion), the strongest correlation is found between yield and final surface sizes, $\rho(N_0, N_1) = 0.78$, and between the hardening parameter and plastic energy dissipated before necking occurs, i.e. $\rho(k_F, W_{pl}^{1,2}) = -0.72$. For the double-twist, most variables correlate with the wire stiffness ($E \propto EA \propto EI$). Since

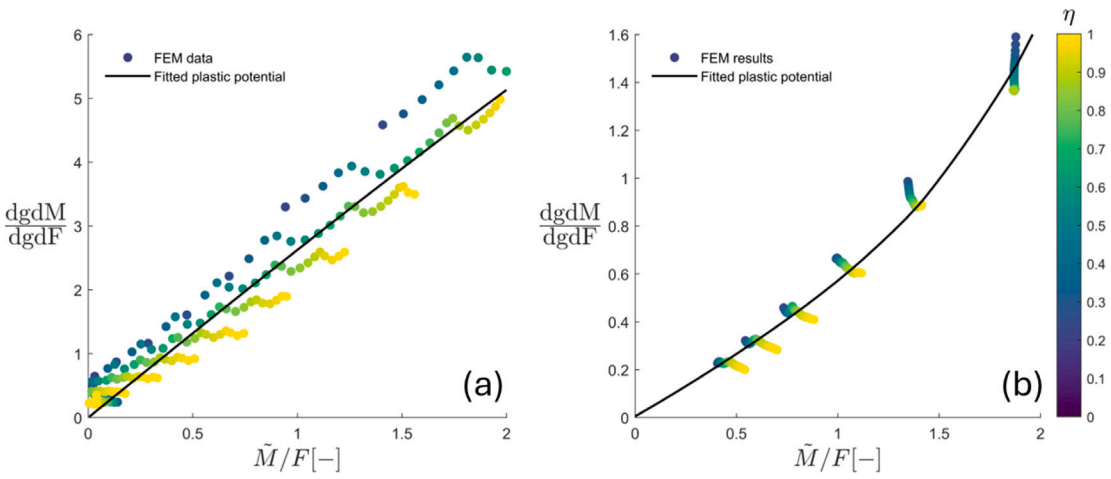

Fig. 7. FEM results and plastic potential best fit. (a) single-wire, (b) double-twist.

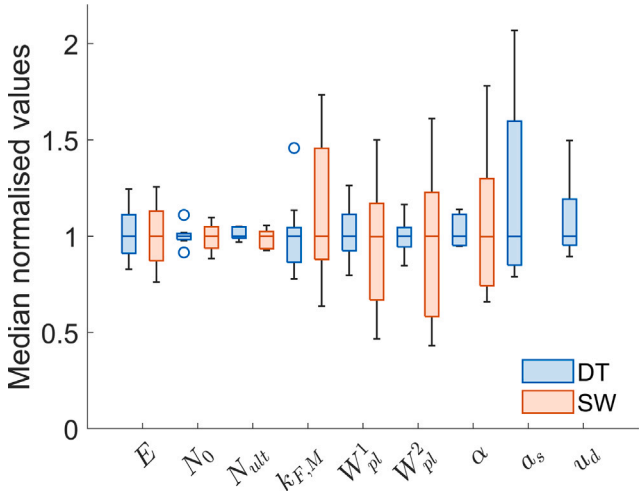

Fig. 8. Coefficient of variation (CV) for the various models parameters.

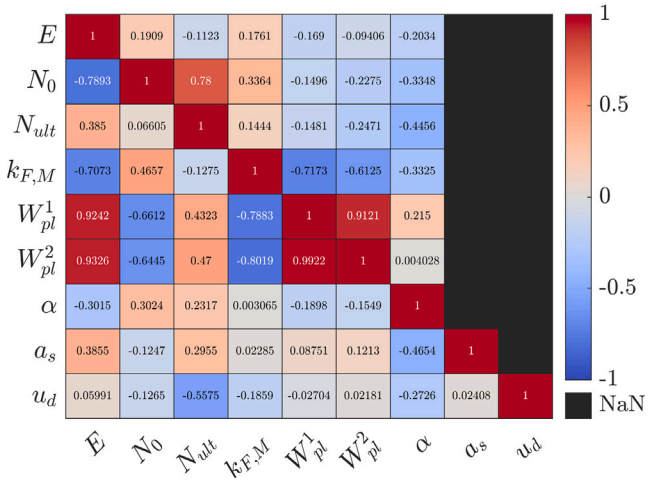

Fig. 9. Correlation matrix for the best-fitting parameters. The upper triangular portion of the matrix corresponds to single-wires, the lower to double-twists.

this variable exhibits low skewness and a quasi-normal distribution in both SW and DT, it is used to assign the rest. Yield surface and plastic potential shape parameters are here considered characteristic of the double-twisted mesh design and are therefore not included in the stochastic model. The fact that the SW stiffness parameters (k_F and k_M) exhibit a significantly higher variability when compared to the DT ones is assumed to be due to the fact that each experimental DT test is in-fact an averaging operation: during a single DT pulling test, four individual single-wire pieces are loaded at the same time. The overall stiffness is therefore averaged, while the failure strength is the one of the weakest connection.

All the following parameters can be calibrated from a single force–displacement curve: the axial stiffness EA is obtained as $\Delta F/\Delta u$ within the linear elastic region of the force–displacement and moment–rotation curves. Yield force N_0 is selected as the transition point between linear and non-linear behaviour, while N_1 is the peak value. The plasticity parameters are fitted on plastic deformation data, obtained from the post-yielding displacements through Eq. (14). Given N_0 and N_1, the plastic portion of the force–displacement curve is converted to $\eta = [0, 1]$ through Eq. (11). The plastic hardening parameter k_F is then obtained by fitting Eq. (12) in $\eta - u_{pl}$ space. In a similar way, the wire damage parameter α is calibrated on the softening portion of the force–displacement curve: the energy dissipated through plastic work W_{pl} is obtained integrating the monotonic portion of the curve, Eq. (17). The onset of necking/shearing damage W^1_{pl} is the value of W_pl corresponding to the peak in the force–displacement curve (N_1), while W^2_{pl} the one at failure. The fitting parameter α is finally obtained from the RHS of Eq. (18), which expresses the force decay in a range between 1 (peak) and 0 (wire failure). Note that the damage function for the DT is fitted on FEM results, as the experimental setup causes the wire to undergo failure at the DT-SW interface, without reaching the stress state required for the failure of the double-twist itself. The compressive buckling limit N_T can be obtained analytically, numerically or, as done here, experimentally from a compression force–displacement curve (Figs. 3c,d). For double-twists, the mesh distortion factor u_d is directly measured from the experimental data as the displacement value that marks the transition from non-linear to linear force–displacement, while a_s is a fitting parameters for Eq. (5) capturing surface friction as the wire–wire contact area increases.

The other parameters require bending and combined loading data, therefore here we use the results from FEM: M^f_f is a parameter than links the width of the yield surface to its height, and tensile to bending yielding. Given N_0, M^f_f is obtained from the yield point in the moment–rotation curve through Eq. (8). The plastic hardening coefficient k_M is then calculated with the procedure outlined for k_F. The shape parameter β^f is then obtained by fitting the yielding points of combined loading in $M/D - F$ space (Fig. 6). The plastic potential parameters (M^g_f, α^g, β^g) are calibrated by minimising the difference between the

function derivatives and the plastic increments from FEM, as described in the plastic potential section. Note that the FEM results used for calibration are not shown in a figure in this document, but are available in Previtali (2023).

3. Model verification

The macroelement model is tested against the standard uniaxial approach (i.e. only prescribing the axial behaviour) under different loading conditions: (i) axial mesh pull, (ii) out-of-plane loading to failure (i.e. mesh punching) and (iii) non-monotonic dynamic loading (i.e. low-energy impact). All tests are carried out using the code PFC7, by placing DEM particles according to the double-twist pattern (Fig. 1b) and generating remote contact interactions (sic. bonds). For the macroelement model, the parameters of the contact model are those reported in Tables 1 and 2. The uniaxial model is implemented through the parallel bond model, which implements standard Euler-beam behaviour (Potyondy and Cundall, 2004; Previtali et al., 2020a). Plastic hardening is implemented by setting the Young modulus of the contact model as the tangent of the experimental piecewise stress–strain curve through a Python script as done in Previtali et al. (2021c). Parameter variability, i.e. Eq. (20), is implemented by shifting the force–displacement curve: the first force point is set to N_0 and the associated displacement is updated to obtain the target stiffness EA. The target hardening parameter k_F is obtained by scaling the strain of the stress–strain curve so that the final data point in the curve corresponds to $\eta > 0.99$ in Eq. (12). Finally, the force corresponding to the last point on the curve is set to N_1.

The two commonly adopted assumptions are tested: negligible shear, bending and compressive stiffness (sic Uniaxial No Shear) is implemented by setting the compressive and shear stiffness in the parallel bond model to zero. In the beam-equivalent stiffness (sic Uniaxial Beam), the shear modulus is obtained from the axial tangential stiffness, assuming $\nu = 0.3$. This simplification can be seen as one-way coupling: axial displacement influences bending and shearing behaviour but not the other way around. The second moment of inertia for the double-twist interaction is here obtained from the equivalent DT radius, $r_{DT} = \sqrt{2 \cdot r_{SW}}$, so that its section area is twice that of a single-wire.

In all models, a linear elastic contact model with a normal stiffness of 100 MN/m, shear stiffness of 25 MN/m and friction of 0.3 is used for the objects interacting with the barrier. In all simulations, a local damping parameter (=0.05) was applied to the individual particles to avoid spurious oscillations. No dashpot-based damping was applied to the contacts.

3.1. Axial mesh pull

This test aims to compare the model performance under axial tension against available laboratory data. The mesh (5 × 8 double-twist hexagons) is connected to the tensile tester by intertwining its ends to two cylindrical rods (1 cm diameter). In the numerical model, the rods are represented through Finite Difference Method (FDM) hexahedral elements, with a 9.1 mm wide and 8.7 mm thick cross section, to match the area ($A = 7.85\text{E}{-5}$ m^2) and second moment ($I = 4.9\text{E}{-10}$ m^4) of their experimental equivalent. The mesh itself is modelled using DEM, i.e. with remote pairwise interactions between particles. The DEM-FDM domains are connected using edge to edge coupling (Breugnot et al., 2016), which uses orthogonal projection to identify the FDM zone in contact with a given particle, preventing the creation of extra contacts when a DEM particle crosses from one FDM element to the next. Since the FDM zones are discretised using linear elements, the mesh size is set equal to the DEM particle diameter, to smooth the contact normals along the curved surface. Particle projection is only enabled on the DEM elements corresponding to the tips of the hexagons, allowing the beams and wires to slide within the entire interweave hexagon, replicating the experimental conditions (Fig. 10a). The material behaviour of the steel rods is captured through von-Mises plasticity, using standard parameters, i.e. Young's modulus of 210 GPa, Poisson's ratio of 0.3 and strength of 150 MPa. In regard to the plastic modulus, two scenarios were tested: elastic-perfectly-plastic behaviour (scenario [1]) and a plastic modulus of 160 GPa (scenario [2]). This results in a total of 5 simulations: one with the Uniaxial No Shear Model and two different beam plasticity tests each (i.e. perfectly plastic and plastic hardening) for the Uniaxial Beam model and for the Macroelement. As the combined mesh and beam response is not known a-priori and it can vary significantly, no pre-defined stop criterion is employed: the Uniaxial No Shear model runs until the mesh undergoes failure at $u \gg 40$ mm, while for the other scenarios, they are stopped once the beams undergo widespread plasticisation (Fig. 10e) or clearly exhibit the formation of a plastic hinge (Fig. 10f), as at that point the combined mesh-beam response is governed by the plasticity model of the beam, which is not the focus of this study.

The Uniaxial No Shear model exhibits physically unreasonable response, Fig. 10d, as rod deformation causes the mesh to collapse towards the centre without opposing resistance. Once the rod curvature prevents the mesh collapse to continue, almost the entire mesh is loaded axially at the same time, resulting in a stiff response with large peak force (Fig. 11). In regard to the Uniaxial Beam and Macroelement, Figs. 10e, f show how the plastic modulus of the beam affects the mesh response: scenario [1] shows continuous beam deformation with constant curvature, while scenario [2] captures the formation of a plastic hinge. Quantitatively, all models match the stiffness of the experimental curve within its elastic portion (i.e. $u < 5$ mm). Beyond this point, the overall mesh response is governed more by the plastic modulus of the rods rather than the model used to describe the mesh itself. Scenario [1] exhibits roughly a perfectly plastic response in the force–displacement curve (Fig. 11), while introducing plastic hardening improves the match with the experimental data. Since the adopted hardening modulus is somewhat arbitrary, the plot is intended to show that qualitatively capturing the displacement field and failure mode (i.e. Fig. 10) produces a match in the force–displacement curve. There is no point in optimising the hardening modulus through back-calculation, as both uniaxial beam stiffness and the Macroelement can be made to match the experimental curve by tinkering with this parameter.

3.2. Quasi-static punch

This test aims to evaluate the model response to out-of-plane loading up to failure. The model is constituted by a 3 × 3 m mesh panel pinned at its edges (fixed displacements, free rotations) and displaced for a distance of ≈ 0.7 metres at its centre using a flattened semi-circular plate with a radius of 0.5 m and a thickness of 0.15 m (Pol and Gabrieli, 2021).

Fig. 12 plots the reaction force on the platter versus its displacement, while Fig. 13, shows the force distribution within the mesh at failure. As observed in the axial loading test, the zero-shear uniaxial model exhibits the least stiffness whilst achieving the highest peak resistance. The force-chains align with the double-twist orientation until failure initiates at the centre of the mesh, i.e. Fig. 13a, followed by rapid unloading as the rip propagates to the edges of the platter (Bertrand et al., 2008). Depending on the initialisation values of the random parameters within the mesh, the rip can also propagate in an inclined direction in respect to the double-twist orientation (Previtali, 2023). Despite their initial similar trends in the force–displacement curve, the Macroelement and the Uniaxial Beam models undergo different failure mechanisms. As out-of-plane bending and shearing increases, the former undergoes plasticity and fails at roughly half the peak force achieved by the latter. Both produce a cross-shaped force-chain pattern connecting the corners of the mesh to its centre, also observed in other mesh designs (Hu et al., 2021).

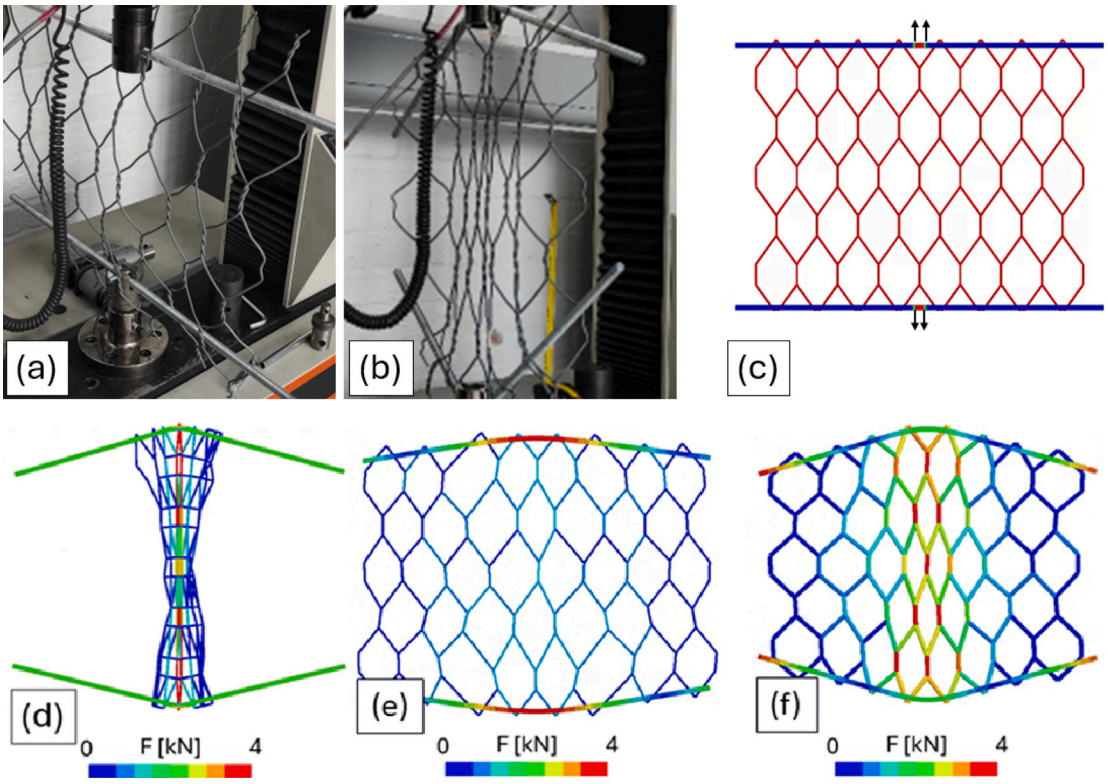

Fig. 10. Experimental setup: (a) initial and (b) final conditions. Numerical model: (c) initial conditions for all the tests. Final state for the uniaxial model with (d) zero bending stiffness mesh model. Uniaxial beam model: (e) perfectly plastic (scenario [1]) and (f) plastic hardening (scenario [2]) rod model.

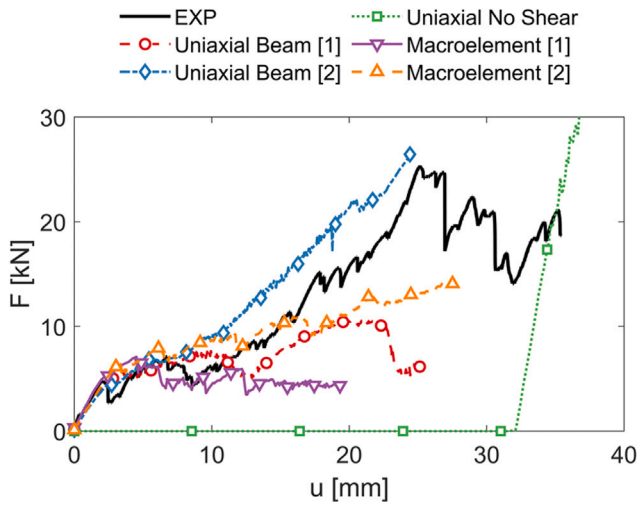

Fig. 11. Force–displacement curves for the pull test. The number next to the mesh model indicates the rod material scenario, i.e. [1] perfectly plastic, [2] plastic hardening.

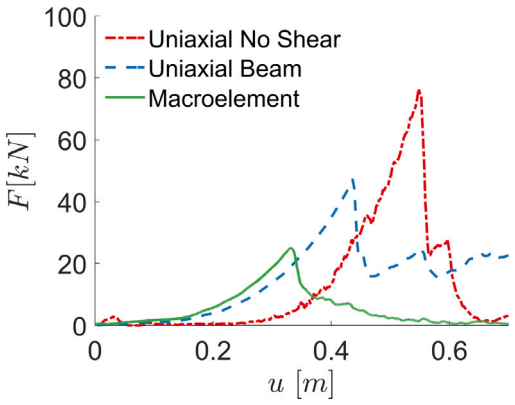

Fig. 12. (a) Force–displacement curves for the punch test.

However, the overly stiff behaviour of the Uniaxial Beam model further concentrates the stress within this area, producing a very localised and brittle failure. The rip propagates in the mesh along the direction normal to the double-twist orientation, pushing the cross-shaped force chain towards the edges of the mesh and unloading the wires on both sides of the rip. In the Macroelement, wire failure occurs concurrently in the zone of maximum mesh elongation (i.e. the centre of the platter) and of maximum curvature (i.e. the edge of the platter), producing a smoother drop in resistance and dis-homogeneous failure pattern.

Overall, the Macroelement model is the only one that exhibits a failure mode with a significant curvature in the deformation field, which in turn increases the risk of mesh puncturing, i.e. the bullet effect. In the uniaxial no shear model, the wires easily undergo bending, but they do not transmit significant force to the platter until they are completely loaded in tension. The beam-equivalent stiffness model produces a similar linear displacement field: as the wires cannot plasticise in shear mode, the mesh behaves as a rigid panel split into two portions.

3.3. Dynamic impact

This test aims to assess the model performance under dynamic conditions, by comparing the numerical results to a laboratory test carried out in Previtali (2023).

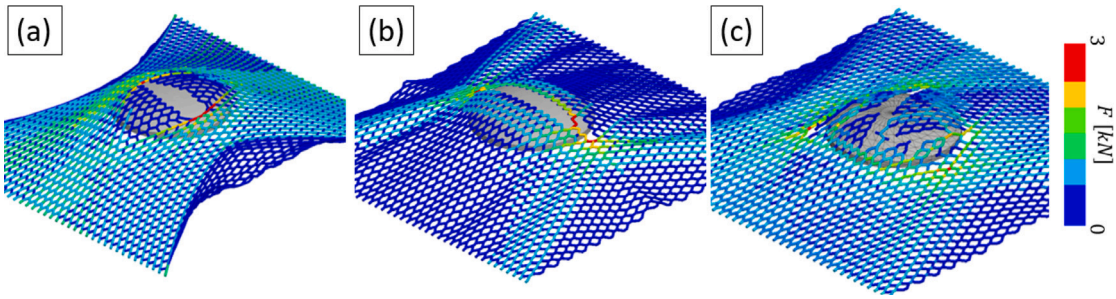

Fig. 13. Mesh failure patterns in the punch test. (a) Uniaxial No Shear, (b) Uniaxial Beam, (c) Macroelement.

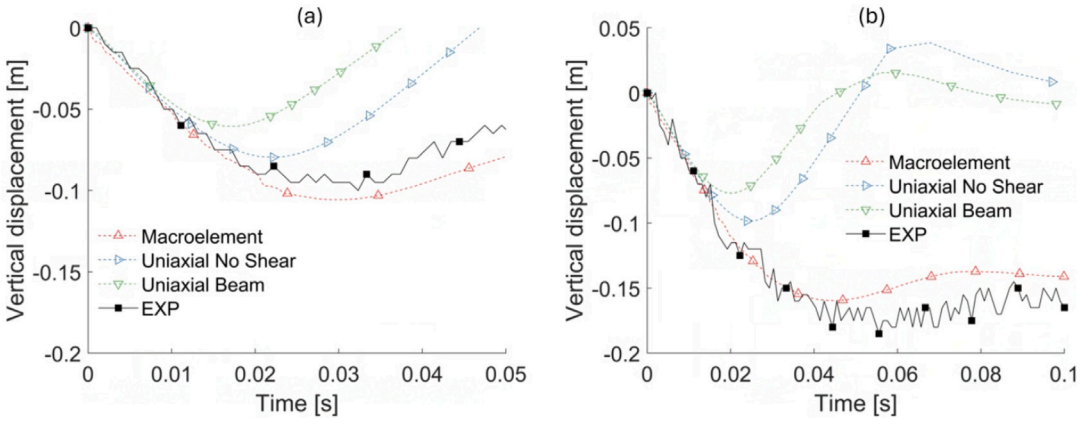

Fig. 14. Vertical displacements against time in the closest marker in proximity of the impact position (a) 5 kg (b) 9 kg mass scenario.

The experimental setup is constituted by a pre-tensioned mesh, fixed to a horizontal frame, impacted by a free-falling block. Mesh deformation is monitored by tracking a large number of individual markers, using a stereo-camera approach to position them in three-dimensional space, and through an Inertial Measurement Unit (IMU) (Previtali, 2023). The mesh, 15×12 hexagons, is pre-tensioned by pulling it in the direction normal to the double-twist orientation until sag is no longer visible. All edges are then stapled to an horizontal wooden frame of 1.12×1 m length (major axis orthogonal to the double-twist direction). A black cloth is then laid on top of the mesh panel to improve contrast for image analysis and marker tracking. The impacting block is a sphere with diameter of 23 cm, released from an elevation of 1.8 m above the mesh, resulting in a speed of ≈ 6 m/s. Two ball masses are tested: 5 and 9 kg, corresponding to a kinetic energy at impact of ≈ 90 and 160 J. In the former, the elastic response of the barrier, i.e. rebound, caused the black cloth to slip out, affecting data acquisition after $t > 0.05$ s. The 5 kg scenario resulted in a residual sag in the centre of the mesh of ≈ 5 cm, while a value of ≈ 15 cm was measured in the 9 kg one. Unfortunately, the successive 9 kg impact occurred close to the edges of the barrier, snapping the staples and causing a crack to propagate through the frame, thus ending the testing campaign. Until this point, the frame did not exhibit any damage (i.e. the staples did not show visible displacement or splintering). Since the frame did not exhibit damage or deformation until the last test, it is not modelled as a deformable body but it is implemented directly as boundary condition, by fixing both displacements and rotations in the particles at the domain edges, after replicating the experimental pre-tensioning procedure.

Fig. 14 shows the vertical displacement profile in the mesh centre against time, while Fig. 15 along the two horizontal axes at peak deformation. The time profile of vertical mesh displacement is taken from the closest marker (Fig. 16a). On the other hand, the displacement profiles against distance are obtained by fitting the available data with a LOcally WEighted Scatterplot (lowes) smoothing function due to the limited number of markers and are therefore a result of extrapolation.

The following observations can be made. First, all models overestimate the curvature of the displacement profile near the impact position. This can be ascribed to the relatively coarse mesh discretisation with the respect to the impacting body, which limits the contacts to 2–3 DEM elements near the mesh centre. Better results can be achieved by increasing the spatial resolution of the mesh discretisation (i.e. increasing the number of DEM particles) and scaling the hardening parameters by the particle to particle distance in order to retrieve the correct stress–strain relationship. As observed in the previous tests, the deformation profile produced by the uniaxial models is almost linear. Since this test is non-monotonic (i.e. the impacting block rebounds), this causes the model to overestimate the elastic response of the barrier, thereby underestimating the amount of plastic dissipation (Fig. 14). Additionally, the Macroelement exhibits a significant deformation anisotropy (Figs. 15, 16), which becomes more evident as the impact force increases.

4. Summary and conclusions

This paper presents a novel constitutive model to simulate double-twisted hexagonal meshes, built upon the widely adopted phenomenological multi-scale framework used to simulate barriers undergoing large deformation. The model is developed by first characterising the mechanical behaviour of the individual mesh wires and using the resulting data to calibrate and verify a Finite Element model of the wire interweaves. This is used to produce a synthetic dataset for loading conditions difficult to obtain experimentally. The Macroelement model is built on this dataset, adopting a standard plasticity framework, with isotropic hardening and a non-associated flow rule. This specific framework was adopted to link the model parameters to physical characteristics such as elastic stiffness, yield and failure load. Assuming that the plastic potential parameters are a characteristic of the mesh design, the other parameters can be calibrated from a tensile and a bending test, as described in the parameter calibration section. Therefore, multiple individual wire tests can be used to characterise

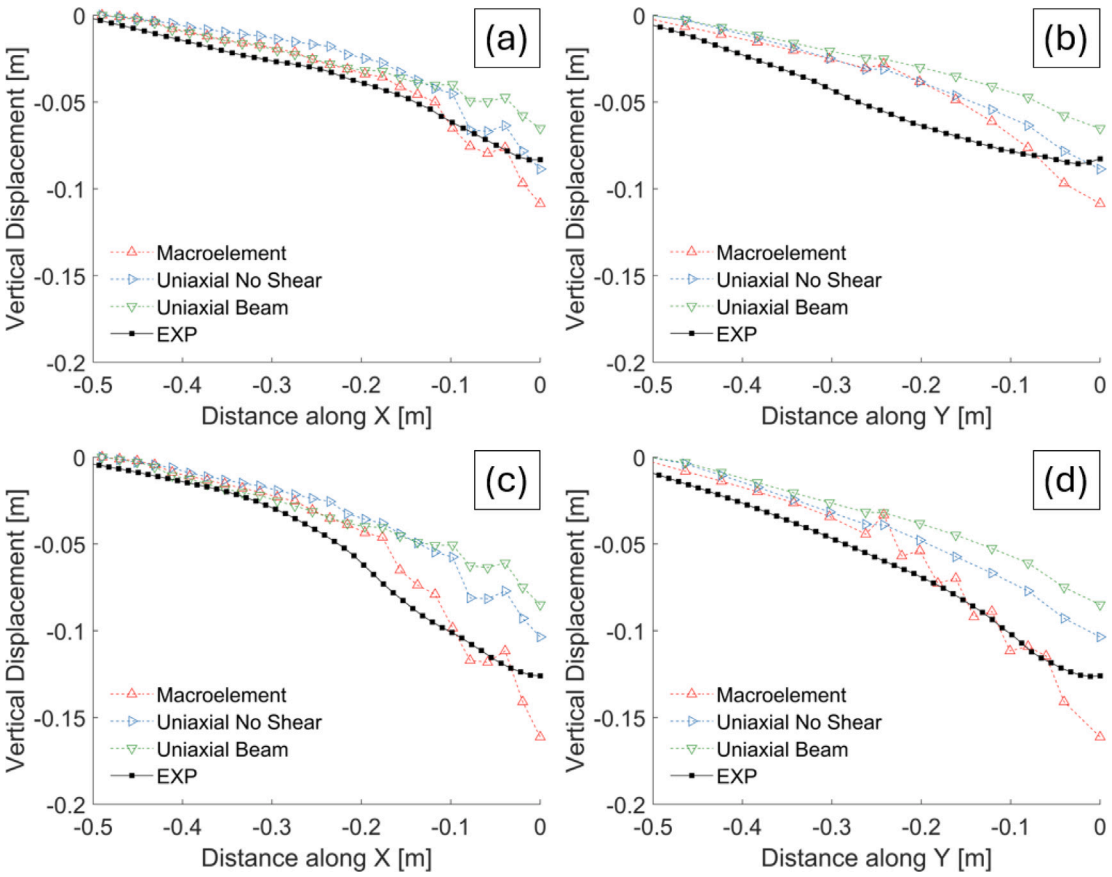

Fig. 15. Maximum vertical displacements against distance from the impact position. (a) parallel and (b) orthogonal to the double-twist orientation, 5 kg scenario. Similarly, (c) and (d) show the parallel and orthogonal displacement for the 9 kg one.

the variability and correlation of each parameter, incorporating for the natural variability of the wires in the meso-scale model. Still, the macroelement equations are versatile enough to allow future users to recalibrate them through the same synthetic dataset approach.

Finally, the proposed model is tested against the standard uniaxial force–displacement approach by implementing both approaches in a DEM framework. The two most commonly adopted scenarios are considered for the uniaxial model: negligible shear stiffness and beam-equivalent behaviour. While these two scenarios produce significant variations in the mesh stiffness, both underestimates the development of localised plasticity, overestimating the final barrier capacity. While it is possible to back-calculate a stiffness ratio that minimises the meso-scale error (Previtali et al., 2021b), this approach provides no predictive information for complex loading scenarios. The proposed model should therefore be adopted when trying to predict the barrier response to non-axial loading conditions, and specifically for situations in which localised plasticity is expected, such as bullet effect scenarios, non-centred impacts and strong interactions with structural elements (e.g. anchor plates in active rockfall mitigation systems).

CRediT authorship contribution statement

Marco Previtali: Writing – original draft, Software, Methodology, Investigation, Formal analysis, Conceptualization. **Matteo Oryem Ciantia:** Writing – review & editing, Supervision, Methodology, Conceptualization. **Giovanni Battista Crosta:** Writing – review & editing.

Funding

The first author acknowledges scholarship funding from the University of Milano-Bicocca and the University of Dundee for supporting their PhD studies. Part of this work was supported by the RESILIENT - Risk Evaluation and Smart Implementation of Landslides monItoring by Citizen Engagement and New Technologies - project funded by Fondazione Cariplo.

Declaration of competing interest

The authors declare that they have no known competing financial interests or personal relationships that could have appeared to influence the work reported in this paper.

Acknowledgements

Tony Bailey from Geobrugg is gratefully acknowledged for fruitful discussions. The authors also thank Geo-Rope Ltd for providing the steel meshes.

Appendix A

A.1. Implementation details

In this model, force and bending moment are respectively defined as signed and unsigned scalars. Therefore, a few manipulations are required to map them to the three-dimensional DEM environment. The macroelement variable F corresponds the axial component of the force vector of a given contact. The two shear components are obtained through standard beam theory, i.e. $\delta S = \delta u_s \cdot GA$, where G is the secant shear modulus of the material, obtained from N_f (instead of F). This has the effect of causing the shear stiffness of the wire to degrade based on its bending history, indirectly introducing plasticity in shear. In

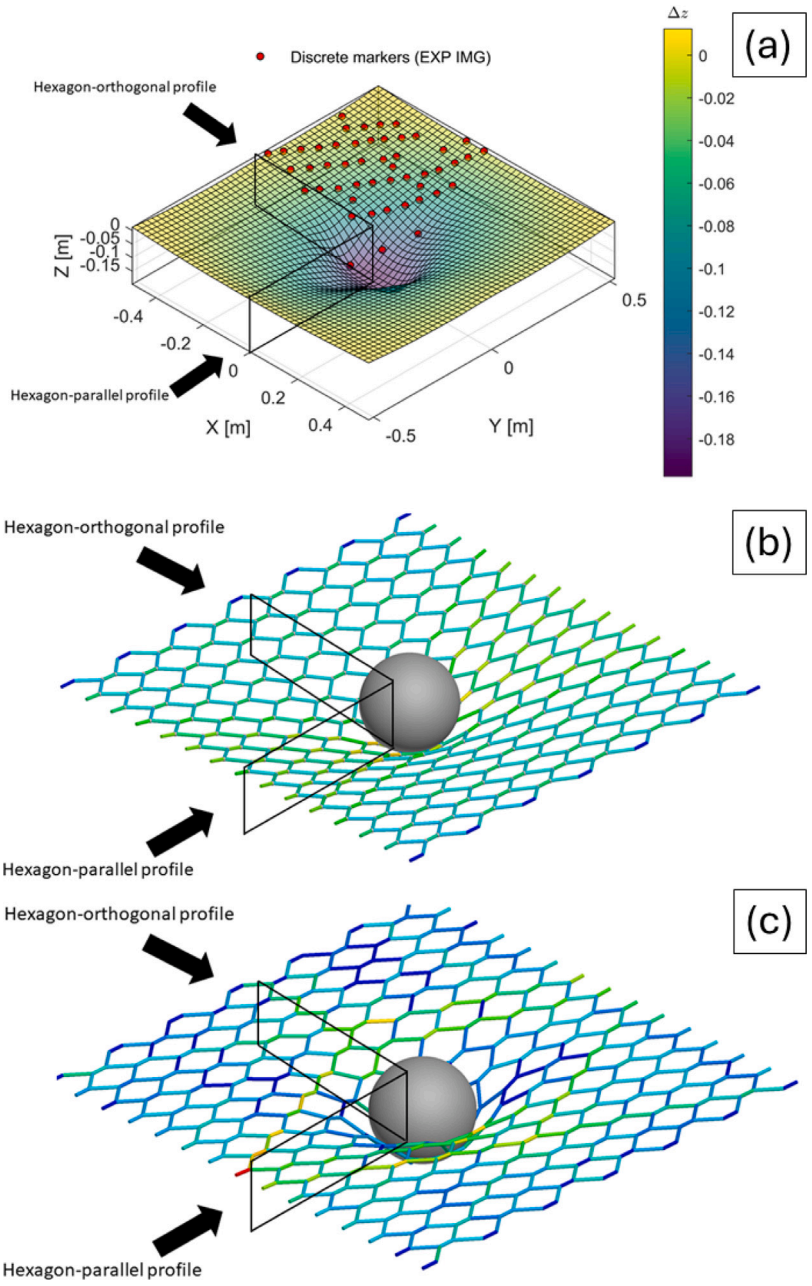

Fig. 16. Final state in the 9 kg block case. (a) experimental displacements map. Mesh deformation in the simulation, using (b) uniaxial no shear, (c) Macroelement model.

regards to moment, its twisting component is considered negligible and it also solved elastically through the updated shear modulus. Stiffness is assumed uniform in the two bending modes, as this was observed in FEM results (Previtali, 2023). The sign of the moment and rotation increments are stored and used to check whether the increment crosses the zero value, i.e. the sign flips. In this case, the bisection algorithm is used to identify the zero-moment value and to obtain the final trial moment (through Pythagoras' theorem). This process is then repeated evaluating the yield surface at trial moment and force. This nested loop can cause significant computational burden in the relatively common scenario of moment causing yielding in one direction and near-zero oscillations in the other. Therefore, an additional simplification is adopted, by assumed that bending is only significant in one direction (e.g. the rotation axis is orthogonal to the double-twist orientation in Fig. 1); and the same secant stiffness approach used for shear force is adopted for the out-of-plane direction. Non-linear plasticity is solved with an explicit Runge–Kutta method of third order and error control.

A.2. Wire friction

The initial low-stiffness double-twist behaviour can be obtained analytically using Herzian contact theory: given the wire-normal force P, the contact areas (A) between two cylinders of equal radius (r), and elastic parameters (E, ν) depends on their relative orientation, with limit cases of circular (Eq. (22)) and rectangular (Eq. (23)) contacts, for orthogonal and parallel wires, respectively.

$$E_c = \frac{E}{2(1-\nu^2)} \tag{21}$$

$$A = \pi \left(\frac{3Pr}{4E_c} \right)^{2/3} \tag{22}$$

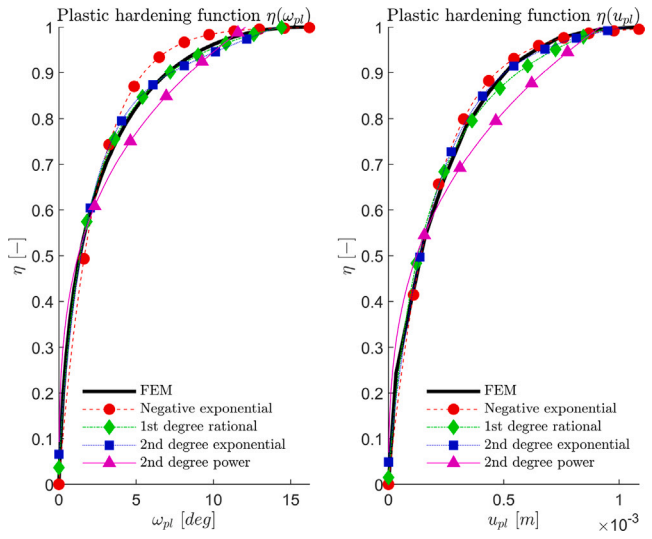

Fig. 17. Plastic hardening function for the single-wire yield surface evolution (FEM data), from Previtali (2023).

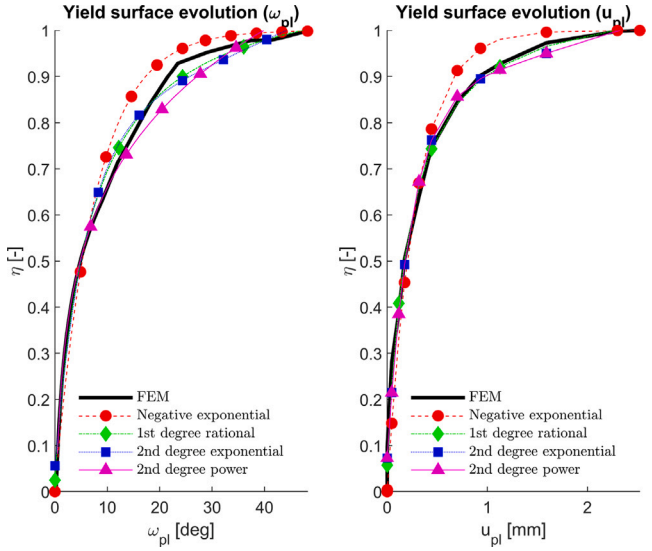

Fig. 18. Plastic hardening function for the double-twist yield surface evolution, from Previtali (2023).

$$A = L' \left(\frac{4Pr}{\pi E_c} \right)^{1/2} \tag{23}$$

The contact length L' can be calculated from that of the interweavement (L) and number of turns ($n = 1.5$), according to Eq. (24)

$$L' = \sqrt{(2\pi nr)^2 + L^2} \tag{24}$$

The intermediate cases represent an elliptical surface. While computing this analytically is complex, it can be approximated by a circular surface (Eq. (22)), scaled with pre-compiled correction factors (Johnson, 1987).

A.3. Comparison of hardening fitting laws

The following general form equations are used to fit the experimental (axial) and numerical (bending) data, whereby the coefficient of determination R^2 denotes the robustness of the fit. For each function, higher degree formulations, e.g. 2nd degree rational, have also been tested. The ones reported are the lowest degree ones that preserve the fit quality.

Table 3
Plastic hardening functions for the single-wire (FEM)

Function	Parameter	$f(\omega_{pl})$	$f(u_{pl})$
Negative exponential	k	0.419	4916
Negative exponential	R^2	0.9726	0.9922
1st degree rational	P1	1.1217	1.1851
1st degree rational	P2	0.0665	2.678e−6
1st degree rational	Q1	1.8315	1.808e−4
1st degree rational	R^2	0.9983	0.9955
2nd degree exponential	a	0.8301	9.38e−4
2nd degree exponential	b	0.0132	6.72e−2
2nd degree exponential	c	−0.764	−8.89e−4
2nd degree exponential	d	−0.554	−5.017
2nd degree exponential	R^2	0.9945	0.9958
2nd degree power	a	0.5576	9.768
2nd degree power	b	0.2694	0.3185
2nd degree power	c	−0.0914	−0.0528
2nd degree power	R^2	0.9634	0.9671

Table 4
Plastic hardening functions for the double-twisted interweavement.

Function	Parameter	$f(\omega_{pl})$	$f(u_{pl})$
Negative exponential	k	0.2637	4077
Negative exponential	R^2	0.9588	0.9356
1st/2nd degree rational	P1	1.124	120.38
1st/2nd degree rational	P2	0.144	0.8129
1st/2nd degree rational	P3	N/A	0.0121e−4
1st/2nd degree rational	Q1	2.895	0.746e−4
1st/2nd degree rational	R^2	0.9971	0.9908
2nd degree exponential	a	0.79	0.738
2nd degree exponential	b	0.01168	163.4
2nd degree exponential	c	−0.7211	−0.678
2nd degree exponential	d	−0.4	−7820
2nd degree exponential	R^2	0.9937	0.9782
2nd degree power	a	0.5039	4.88
2nd degree power	b	0.2685	0.2419
2nd degree power	c	−0.09348	−0.0435
2nd degree power	R^2	0.971	0.99

- Negative exponential: $\eta = 1 - exp(-k \cdot x)$
- 1st degree rational: $\eta = \frac{P1 \cdot x + P2}{x + Q1}$
- 2nd degree exponential: $\eta = a \cdot exp(b \cdot x) + c \cdot exp(d \cdot x)$
- 2nd degree power: $\eta = a \cdot x^b + c$

where x is the generalised plastic displacement, i.e. u_{pl} and ω_{pl}, while all the other variables are curve fitting parameters. Tables 3 and 4 list the best fitting parameters and R^2 value for each, while Figs. 17 and 18 are the associated plots. The second degree exponential function appears to have the most consistent performance across all datasets.

Appendix B. List of derivatives

$$\frac{\partial N_f}{\partial u_{pl}} = 2k_f \exp(-k_m\omega_{pl} - k_f u_{pl})(N_1 - N_0) \tag{25}$$

$$\frac{\partial N_f}{\partial \omega_{pl}} = 2k_m \exp(-k_m\omega_{pl} - k_f u_{pl})(N_1 - N_0) \tag{26}$$

Compressive subdomain, given $M_Y = N_f D\sqrt{M_f}/2$ and $f = g$:

$$\frac{\partial f}{\partial F} = \frac{2FM_Y}{DN_t^2} \tag{27}$$

$$\frac{\partial f}{\partial M} = \frac{2M}{DM_Y} \tag{28}$$

$$\frac{\partial f}{\partial N_f} = \left[\left(\frac{F^2}{N_t^2} + \frac{M^2}{M_Y^2} - 1 \right) - \frac{2M^2}{M_Y^2} \right] \sqrt{M_f}/2 \tag{29}$$

Tensile subdomain, given $F^* = F - N_f/2$ and $F^\dagger = F - N_f/2$:

$$\frac{\partial f}{\partial F} = hM_f \left[F^\dagger + F^* - \frac{F^\dagger (F^*)^2}{\alpha(N_f\beta)(N_f - \alpha)} \right] \tag{30}$$

$$\frac{\partial f}{\partial_M} = \frac{2M}{D^2} \tag{31}$$

$$\frac{\partial f}{\partial N_f} = hM_f \left[\alpha(F^\dagger - F^*) + \frac{F^\dagger F^*}{\alpha\beta} \left(\frac{F^*}{N_f} - \alpha \right) \left(\frac{F^*}{N_f^2} - \frac{\alpha}{N_f} \right) \right] \tag{32}$$

Combining the above equations, the plastic multiplier λ is obtained as:

$$\dot{\lambda} = \frac{EA\frac{\partial f}{\partial F}\dot{u} + EI\frac{\partial f}{\partial M}\dot{\omega}}{EA\frac{\partial f}{\partial F}\frac{\partial g}{\partial F} + EI\frac{\partial f}{\partial M}\frac{\partial g}{\partial M} - \frac{\partial f}{\partial N_f}\left(\frac{\partial N_f}{\partial \omega_{pl}}\frac{\partial g}{\partial M} + \frac{\partial N_f}{\partial u_{pl}}\frac{\partial g}{\partial F} \right)} \tag{33}$$

Data availability

The Macroelement code and example applications are available at: https://github.com/marcoprevitali/macroelement-doubletwist-PFC7.

Calibration data is available at: https://zenodo.org/records/17299219.

References

Abaqus, G., 2011. Abaqus 6.11. Dassault Systemes Simulia Corporation, Providence, RI, USA.

Al-budairi, H., Gao, Z., Steel, A., Wheeler, S., Davies, T.R., 2016. Modelling and Optimising of a Light-Weight Rockfall Catch Fence System. In: NAFEMS UK Conference 2016. pp. 129–132.

Albaba, A., 2015. Discrete element modeling of the impact of granular debris flows on rigid and flexible structures.

Albaba, A., Lambert, S., Kneib, F., Chareyre, B., Nicot, F., 2017. DEM modeling of a flexible barrier impacted by a dry granular flow. Rock Mech. Rock Eng. 50, 3029–3048.

Bertrand, D., Nicot, F., Gotteland, P., Lambert, S., 2008. Discrete element method (DEM) numerical modeling of double-twisted hexagonal mesh. Can. Geotech. J. 45 (8), 1104–1117.

Boschi, K., di Prisco, C., Flessati, L., 2023. An innovative design approach for anchored wire meshes. Acta Geotech. 18 (11), 5983–6005.

Breugnot, A., Lambert, S., Villard, P., Gotteland, P., 2016. A Discrete/continuous Coupled Approach for Modeling Impacts on Cellular Geostructures. Rock Mech. Rock Eng. 49 (5), 1831–1848.

Di Laora, R., Galasso, C., Mylonakis, G., Cosenza, E., 2020. A simple method for N-M interaction diagrams of circular reinforced concrete cross sections. Struct. Concr. 21 (1), 48–55.

Effeindzourou, A., Thoeni, K., Giacomini, A., Wendeler, C., 2017. Efficient discrete modelling of composite structures for rockfall protection. Comput. Geotech. 87, 99–114.

EOTA, 2013. ETAG 027:2013 Falling Rock Protection Kits. December 1988.

Escallón, J., Boetticher, v., Wendeler, C., Chatzi, E., Bartelt, P., 2015. Mechanics of chain-link wire nets with loose connections. Eng. Struct. 101, 68–87.

Gerolymatou, E., 2017. Induced and Inherent Anisotropy in Rock Mass. Habilitation, Karlsruhe Institut fr Technologie, Karlsruher.

Gossling, T.H., 1981. Bulge, shear and squash: a prepresentation for the general conic arc. Computer-Aided Des. 13 (2), 81–84.

Hu, B., Wu, Y., Wang, H., Tang, Y., Wang, C., 2021. Risk mitigation for rockfall hazards in steeply dipping coal seam: a case study in xinjiang, northwestern China. Geomatics Nat. Hazards Risk 12 (1), 988–1014.

Huang, J., Griffiths, D., 2009. Return mapping algorithms and stress predictors for failure analysis in geomechanics. J. Eng. Mech. 135 (4), 276–284.

Johnson, K.L., 1987. Contact Mechanics. Cambridge University Press.

Lagarias, J.C., Reeds, J.A., Wright, M.H., Wright, P.E., 1998. Convergence properties of the Nelder–Mead simplex method in low dimensions. SIAM J. Optim. 9 (1), 112–147.

Lambert, S., Bourrier, F., 2024. Flexible facing systems for surficial slope stabilisation: A literature review. Geotech. Geol. Eng. 42 (7), 5425–5446.

Li, X., Zhao, J., 2018. A unified CFD-DEM approach for modeling of debris flow impacts on flexible barriers. Int. J. Numer. Anal. Methods Geomech. 42 (14), 1643–1670.

Li, X., Zhao, J., Kwan, J.S., 2020. Assessing debris flow impact on flexible ring net barrier: A coupled CFD-DEM study. Comput. Geotech. 128, 103850.

Marigo, N., Gabrieli, F., Pol, A., Bisson, A., Brezzi, L., 2021. A discrete element framework for the modelling of rock-filled gabions. In: ISRM EUROCK. ISRM, pp. ISRM–EUROCK.

Mentani, A., Giacomini, A., Buzzi, O., Govoni, L., Gottardi, G., Fityus, S., 2016. Numerical modelling of a low-energy rockfall barrier: new insight into the bullet effect. Rock Mech. Rock Eng. 49, 1247–1262.

Mijalković, M., Trajković, M., Milošević, B., 2008. Limit analysis of beams under combined stresses. Facta Universitatis-Series: Archit. Civ. Eng. 6 (1), 75–88.

Mitterer, C., Barbist, R., Björk, T., Sundqvist, M., Bergström, J., Hagler, J., 1997. A comparative study on the evaluation of the tribological behaviour of polymer/zinc coated steel sheets. Wear 210 (1–2), 88–95.

Nova, R., Di Prisco, C., 2003. The macro-element concept and its application in geotechnical engineering. Fond. Superf. Press. L'ENPC/LCPC 389–396.

Pol, A., Gabrieli, F., 2021. Discrete element simulation of wire-mesh retaining systems: An insight into the mechanical behaviour. Comput. Geotech. 134, 104076.

Pol, A., Gabrieli, F., Brezzi, L., 2021. Discrete element analysis of the punching behaviour of a secured drapery system: from laboratory characterization to idealized in situ conditions. Acta Geotech. 1–21.

Potyondy, D.O., Cundall, P.A., 2004. A bonded-particle model for rock. Int. J. Rock Mech. Min. Sci. 41 (8), 1329–1364.

Previtali, M., 2023. Experimental and numerical characterization of double-twisted hexagonal meshes for rockfall protection.

Previtali, M., Ciantia, M., Castellanza, R., Crosta, G., 2020a. Mesh sensitivity in discrete element simulation of flexible protection structures. In: Proceedings of the 2020 Annual Conference of the UK Association for Computational Mechanics. UKACM, Loughborough University.

Previtali, M., Ciantia, M., Castellanza, R., Crosta, G.B., 2020b. Mesh sensitivity in discrete element simulation of flexible protection structures. http://dx.doi.org/10.17028/rd.lboro.12102534.v1.

Previtali, M., Ciantia, M., Spadea, S., Castellanza, R., Crosta, G., 2021a. Development of a macro-element model for rockfall steel wires using experimental and numerical data. In: Proceedings of the 18th UK Travelling Workshop: GeoMechanics: From Micro To Macro (GM3), Dundee, 2021. University of Dundee, pp. 33–36.

Previtali, M., Ciantia, M.O., Spadea, S., Castellanza, R., Crosta, G., 2021b. Discrete element modeling of compound rockfall fence nets. In: Challenges and Innovations in Geomechanics: Proceedings of the 16th International Conference of IACMAG-Volume 2 16. Springer, pp. 560–567.

Previtali, M., Ciantia, M.O., Spadea, S., Castellanza, R.P., Crosta, G.B., 2021c. Multiscale modelling of dynamic impact on highly deformable compound rockfall fence nets. Proc. Inst. Civ. Engineers-Geotechnical Eng. 174 (5), 498–511.

Shigley, J., Mischke, C.R., Budynas, R.G., et al., 1972. Mechanical engineering design.

Simo, J.C., Ju, J.W., 1987. Strain-and stress-based continuum damage models—I. formulation. Int. J. Solids Struct. 23 (7), 821–840.

Spadari, M., Giacomini, A., Buzzi, O., Hambleton, J.P., 2012. Prediction of the bullet effect for rockfall barriers: A scaling approach. Rock Mech. Rock Eng. 45 (2), 131–134.

Steinbrecher, I., Humer, A., Vu-Quoc, L., 2017. On the numerical modeling of sliding beams: A comparison of different approaches. J. Sound Vib. 408, 270–290.

Thoeni, K., Lambert, C., Giacomini, A., Sloan, S.W., 2013. Discrete modelling of hexagonal wire meshes with a stochastically distorted contact model. Comput. Geotech. 49, 158–169.

Thomson, w., 1865. IV. On the elasticity and viscosity of metails. Proc. R. Soc. Lond. (14), 289–297.

Volkwein, A., Vogel, A., Gerber, W., Roth, A., 2011. Brief communication " Tree impacts into a flexible rockfall protection system ". pp. 3047–3051. http://dx.doi.org/10.5194/nhess-11-3047-2011.

Xu, H., Gentilini, C., Yu, Z., Qi, X., Zhao, S., 2018. An energy allocation based design approach for flexible rockfall protection barriers. Eng. Struct. 173, 831–852.